Supplementary Materials

Self-stratified stretchable passive cooling interface for thermal management of on-skin electronics

Jiahao Sun[1,#], Mingzi Liu[2,#], Cancheng Jiang[3,#], Qingqiao Cai[1], Rong Cai[1], Jiahui Li[1], Yawen Xiao[1], Qingyi Xian[1], Xiaonan Sun[1], Lelun Jiang[1], Cheng Li[4], Chi Yan Tso[3], Xinge Yu[2], Yingying Zhou[5,*], Zehua Peng[1,*], Jiyu Li[1,*]

[1]School of Biomedical Engineering, Shenzhen Campus of Sun Yat-sen University, Shenzhen 518107, Guangdong, China.
[2]Department of Biomedical Engineering, City University of Hong Kong, Hong Kong 999077, China.
[3]School of Energy and Environment, City University of Hong Kong, Hong Kong 999077, China.
[4]School of Chemical Engineering and Technology, Sun Yat-sen University, Zhuhai 519082, Guangdong, China.
[5]School of Professional Education and Executive Development, The Hong Kong Polytechnic University (PolyU SPEED), Hong Kong 999077, China.

[#]Authors contributed equally.

[*]**Correspondence to:** Dr. Jiyu Li, Dr. Zehua Peng, School of Biomedical Engineering, Shenzhen Campus of Sun Yat-sen University, Shenzhen 518107, Guangdong, China. E-mail: lijy887@mail.sysu.edu.cn; pengzeh@mail.sysu.edu.cn; Dr. Yingying Zhou, School of Professional Education and Executive Development, The Hong Kong Polytechnic University (PolyU SPEED), Hong Kong 999077, China. E-mail: july.zhou@cpce-polyu.edu.hk

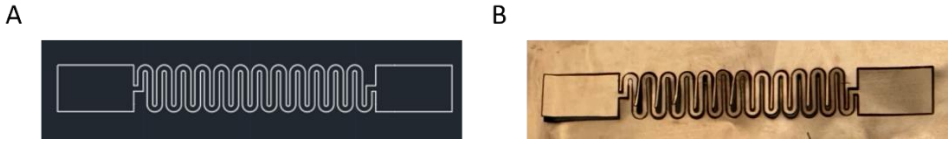

Supplementary Figure 1. Serpentine resistive heater fabrication: (A) serpentine resistive pattern designed in AutoCAD; (B) serpentine resistive element obtained by laser cutting (Photographed by the authors)**.**

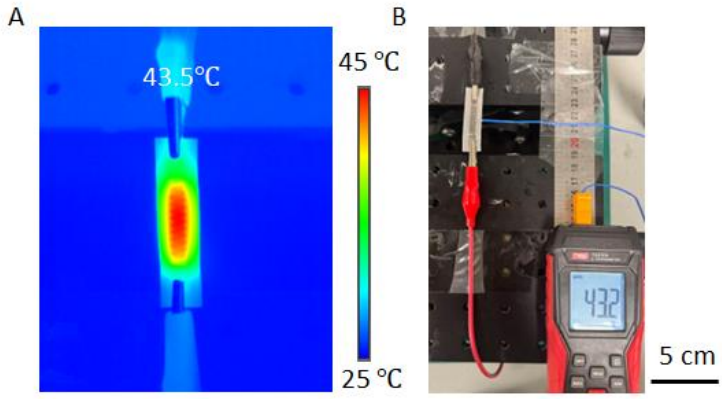

Supplementary Figure 2 Thermocouples Verify the Accuracy of Infrared Thermal Imager Temperature Measurements (Photographed by the authors).

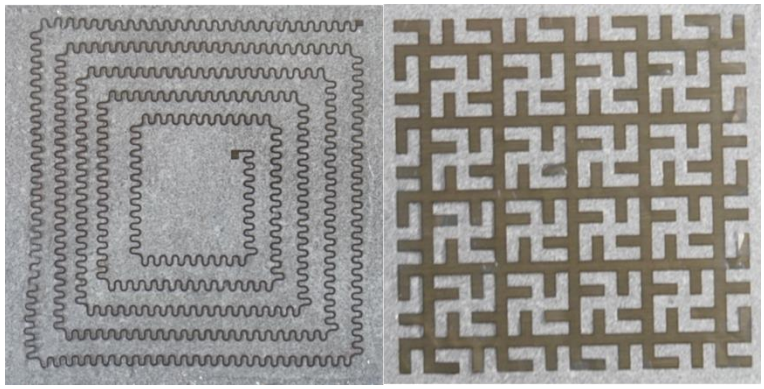

Supplementary Figure 3. SPCI can be integrated with diverse patterns fabricated by different processing methods; as representative examples, SPCI was integrated with a square-spiral (meander) pattern and a windmill pattern (Photographed by the authors).

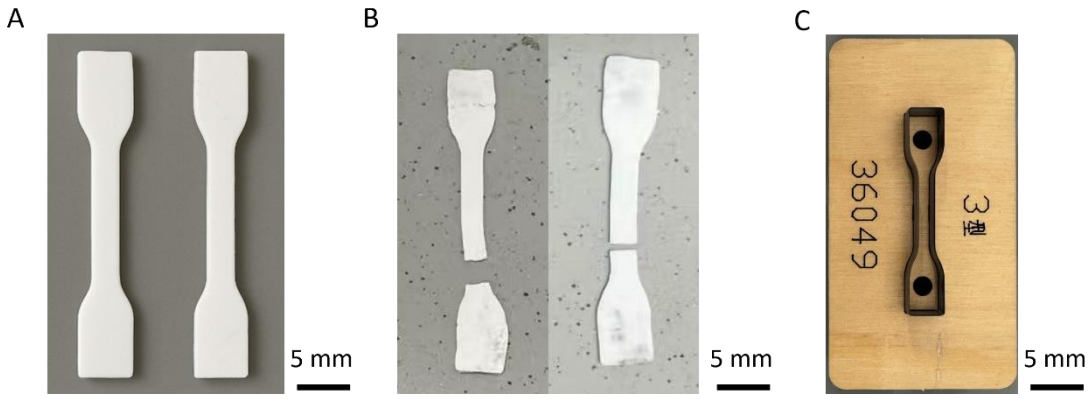

Supplementary Figure 4. Tensile tests were performed on SPCI specimens. (A) Dog-bone-shaped SPCI before stretching; (B) SPCI after fracture; (C) standard dog-bone die for tensile testing (national standard) (Photographed by the authors).

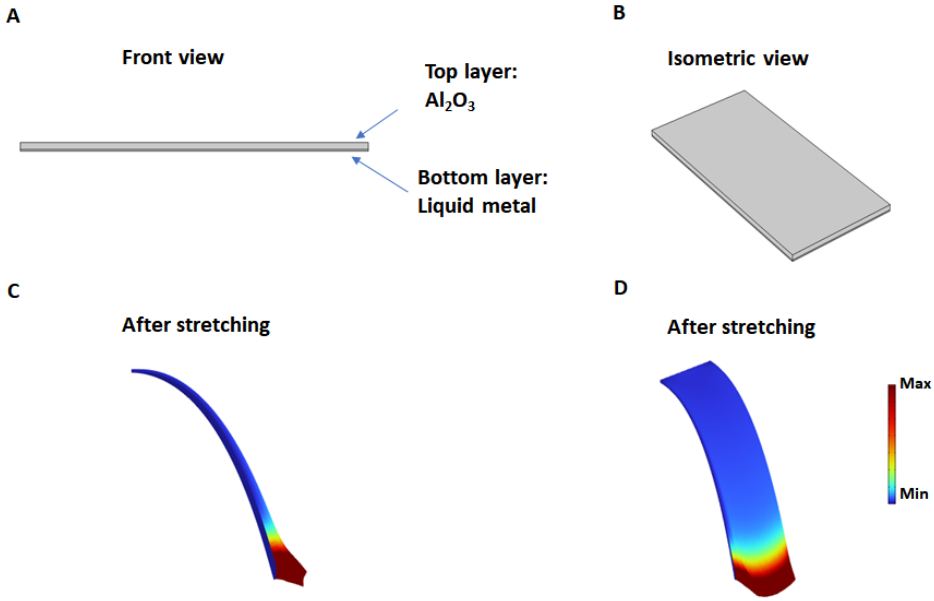

Supplementary Figure 5. Simulation of the stretching stability of liquid metal.

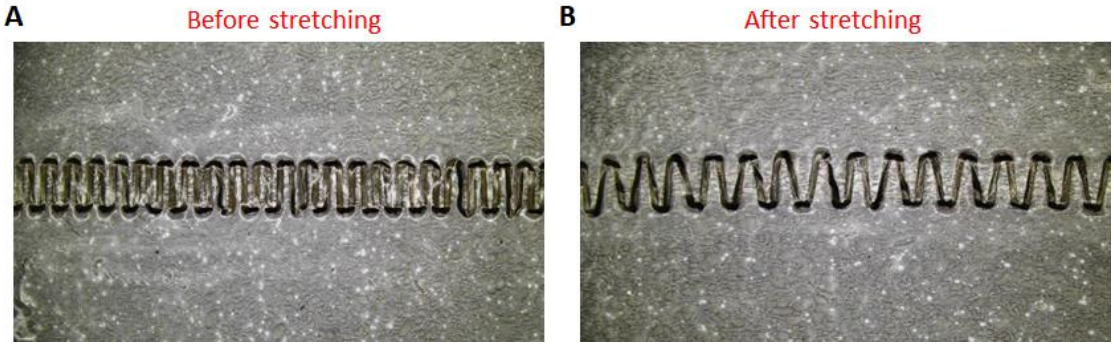

Supplementary Figure 6. Microstructure of the LM network under stretched conditions. A. Before stretching. B. After stretching (Photographed by the authors).

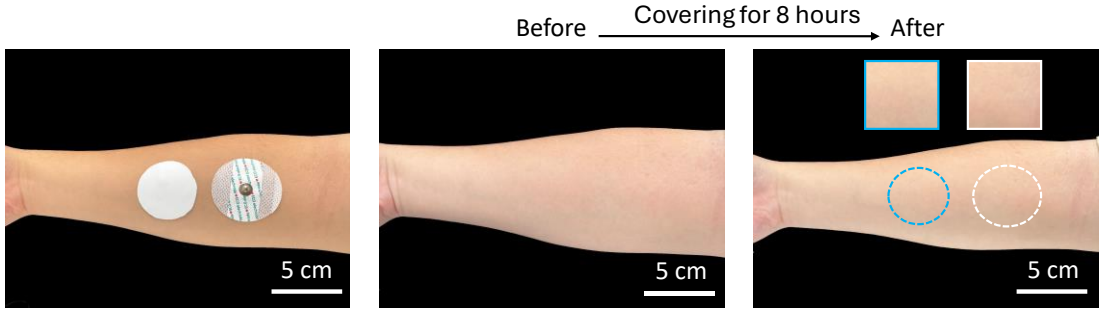

Supplementary Figure 7. SPCI Biocompatibility Testing. After wearing it for 8 hours, the skin showed no signs of redness, swelling, or allergic reactions (Photographed by the authors).

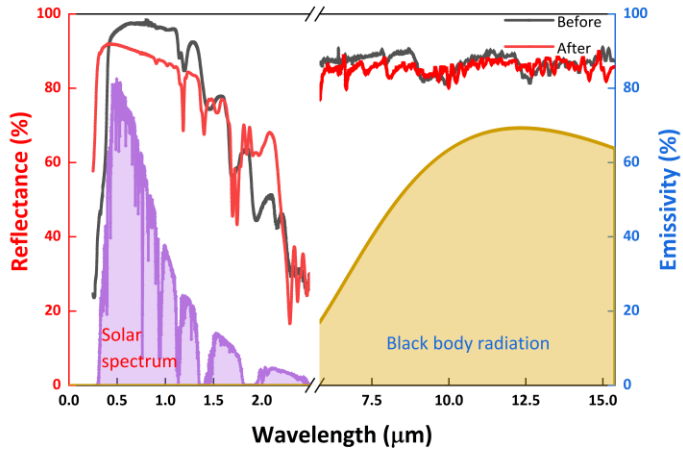

Supplementary Figure 8. Spectral Performance Plots Before and After 1,000 Stretching Cycles.

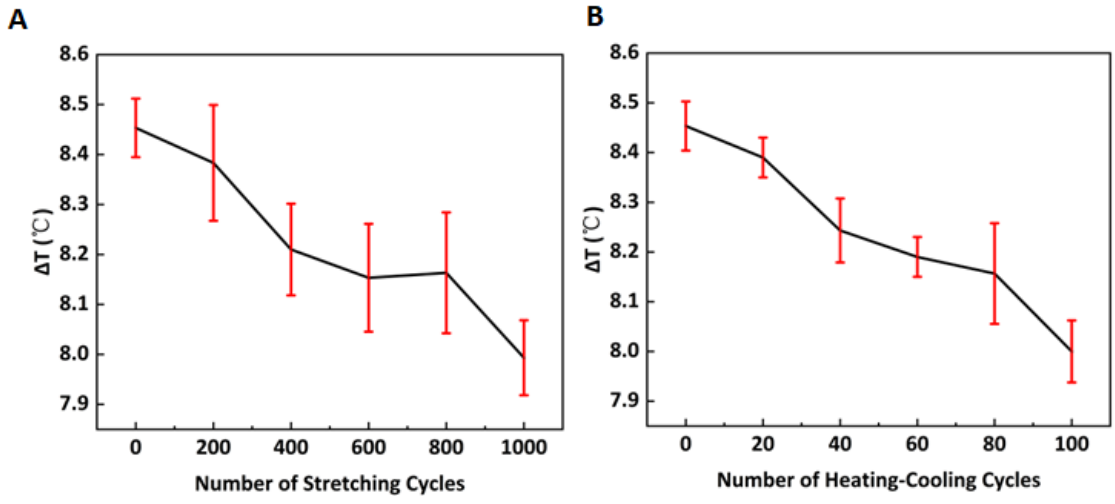

Supplementary Figure 9. Left: Variation in heat dissipation performance under cyclic stretching conditions. Right: Variation in heat dissipation performance under heating/cooling conditions.

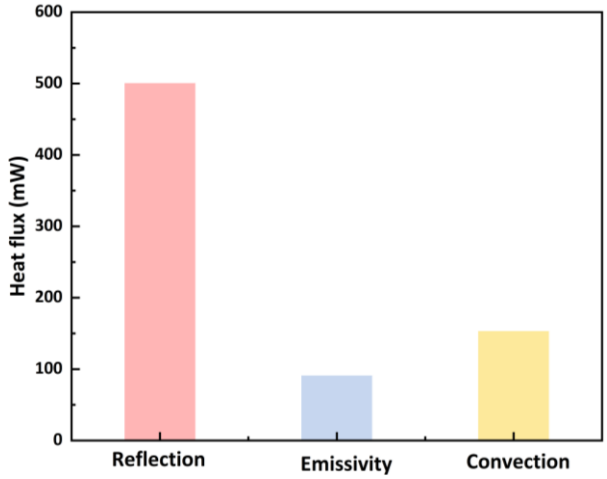

Supplementary Figure 10. The contribution of each cooling mechanism[1–3].

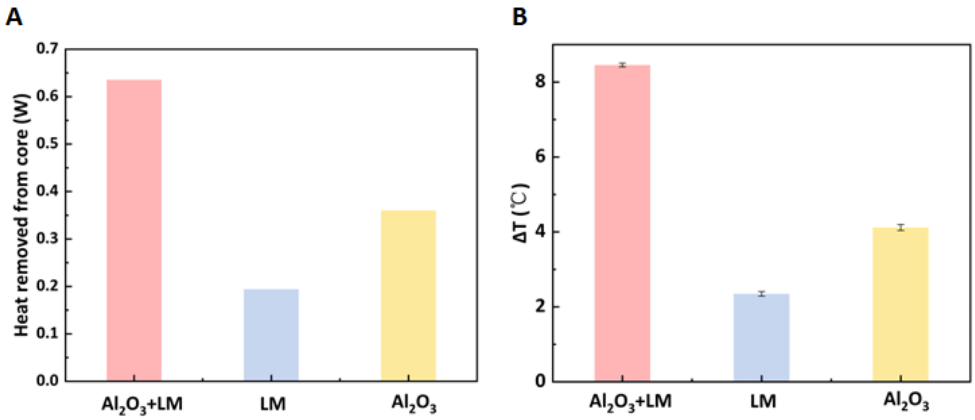

Supplementary Figure 11. The respective contributions of Al_2O_3 and LM to heat removal. B. Cooling performance with both LM and Al_2O_3 present, with LM only, and with Al_2O_3 only.

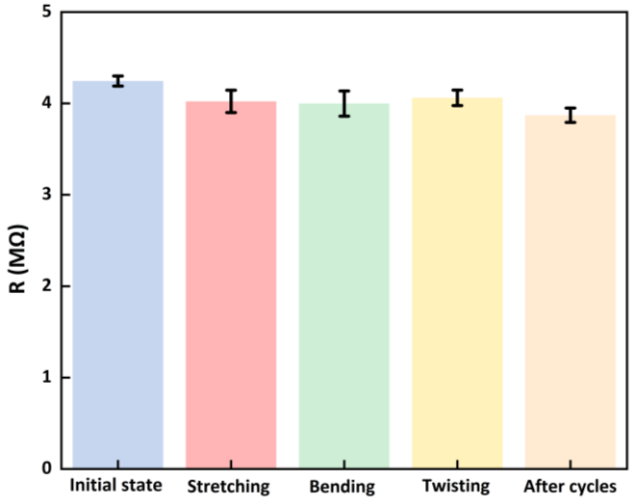

Supplementary Figure 12. SPCI and Circuit Insulation Testing (Change in Resistance Value). After undergoing stretching, bending, twisting, and 1,000 cycles of tensile testing, the insulation performance between the SPCI and the circuit remains excellent.

Supplementary Figure 13. After cyclic stretching, the insulating layer exhibited no visible cracks, nor did the liquid metal migrate into the insulating layer (Photographed by the authors).

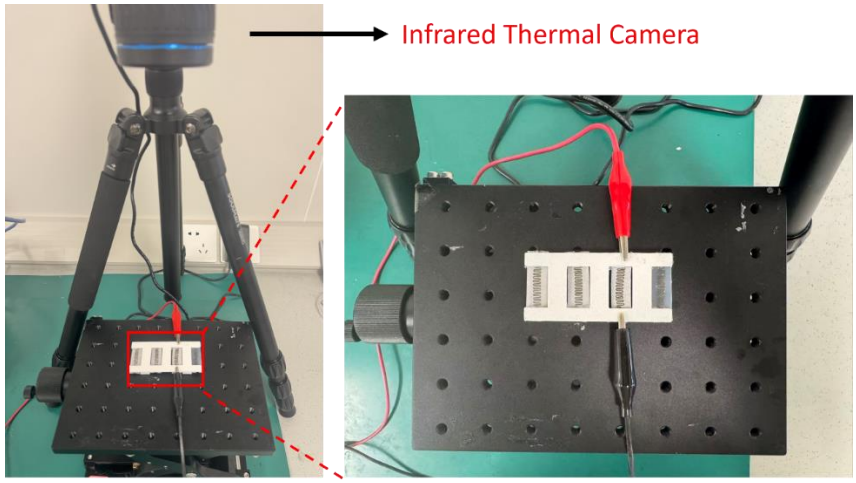

Supplementary Figure 14. Left: the temperature-measurement setup for the serpentine

circuit. Right: a serpentine-array device integrated with SPCI samples containing different liquid metal contents (Photographed by the authors).

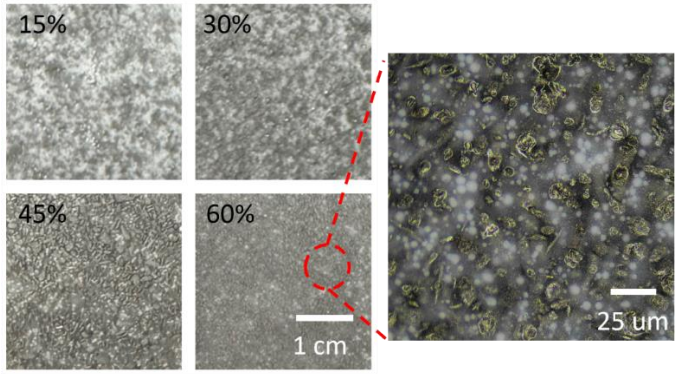

Supplementary Figure 15. Bottom-view images of SPCI with different liquid metal mass fractions; the right panel shows a magnified view of the 60 wt% SPCI region (Photographed by the authors).

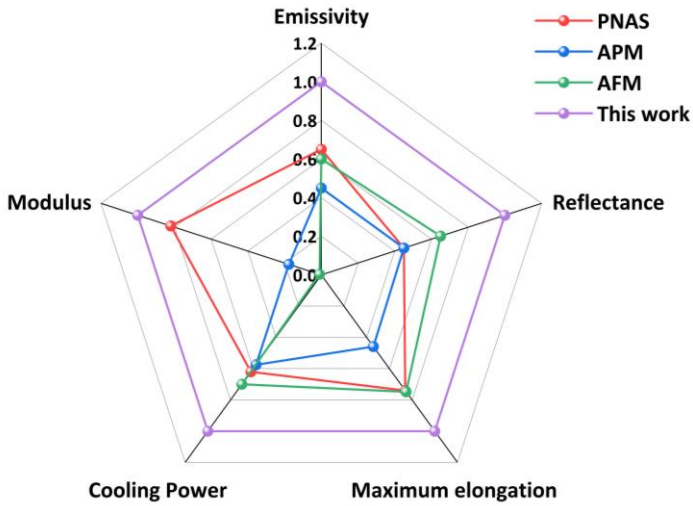

Supplementary Figure 16. Comparation of key metrics reported in recent LM–elastomer composite studies.

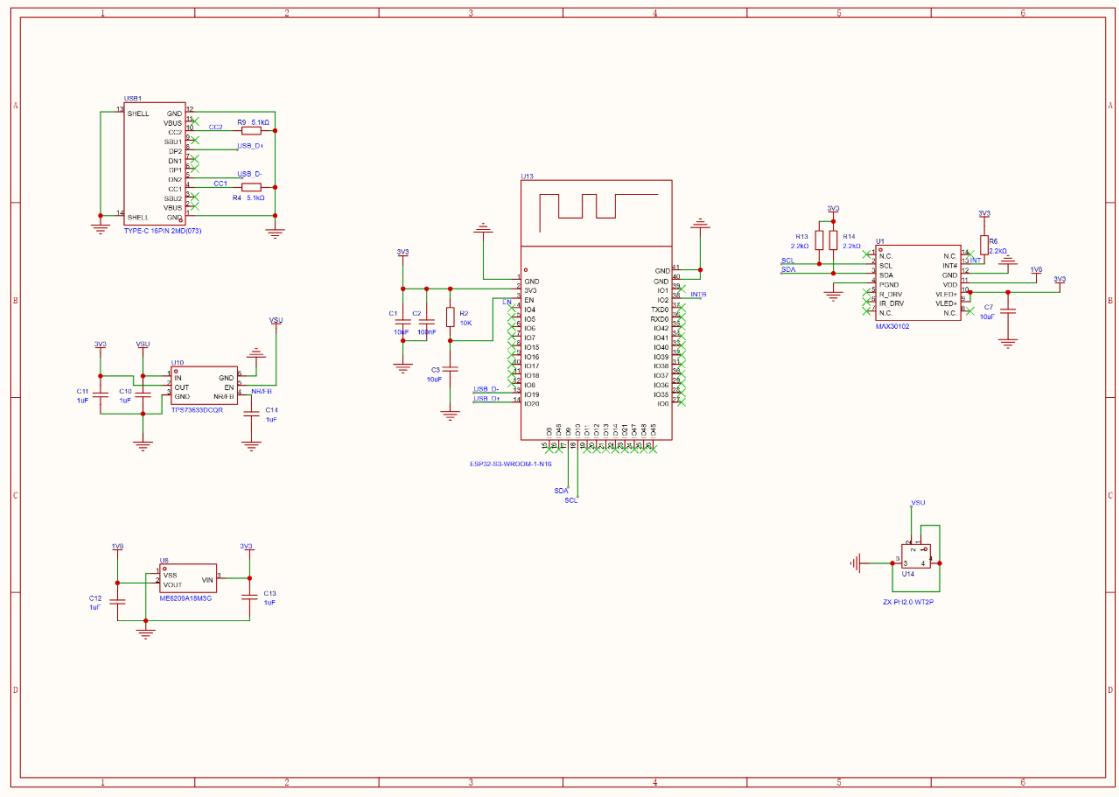

Supplementary Figure 17. Schematic design of the wireless PPG sensing module (main).

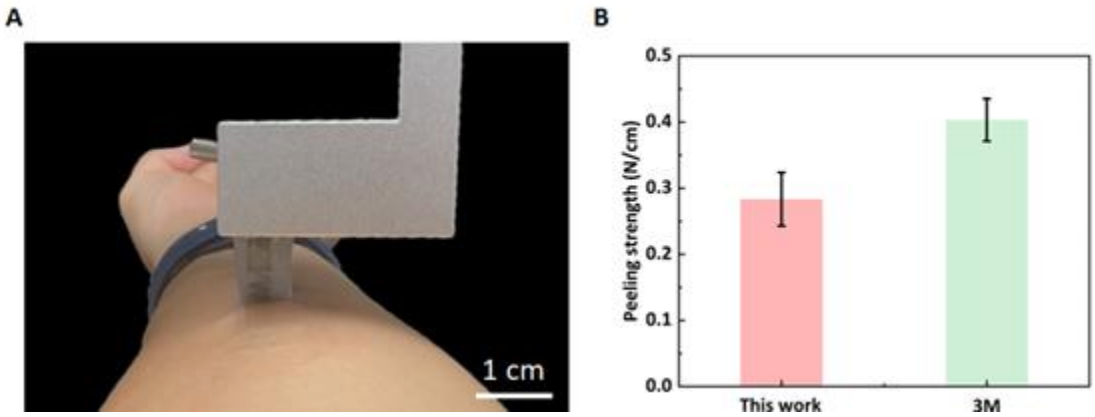

Supplementary Figure 18. Peeling force testing. A. Peel force test setup. B. Peeling strength of this work and 3M (Photographed by the authors).

S1: Details of the optical parameters and simulation settings.

The wavelength-dependent complex refractive index of Al_2O_3 used in the Mie scattering calculations was taken from literature sources[1]. The elastomeric matrix was modeled as a homogeneous medium with a refractive index of $n = 1.40$.

The scattering and absorption coefficients were calculated using Mie theory and subsequently used as inputs for a Monte Carlo photon transport simulation[2]. In the simulation, photons were launched onto a planar slab and tracked through scattering and absorption events until reflection or absorption occurred. The reflectance was determined from the fraction of photons exiting the incident surface.

The simulation employed periodic lateral boundary conditions and an absorbing bottom boundary. Detailed simulation parameters and assumptions are provided in the Supplementary Materials.

S2: Applying Stokes' Principle to estimate sedimentation velocity:

$$v_s = \frac{2}{9}\frac{(\rho_p - \rho_m)gr^2}{\mu}$$

Where:ρ_p: is the particle density (Al_2O_3 particles ~3.95 g/cm³; LM ~6.28 g/cm³); ρ_m: is the matrix density (Ecoflex-30 ~1.04 g/cm³); and r: is the radius (Al_2O_3 particles: 500 nm; LM: 5–10 μm). Assuming a paste viscosity (μ) of 5 Pa·s, the calculated sedimentation distance for Al_2O_3 is 0.86 μm, while the sedimentation distance for the LM is over 600 μm.

S3: Thermal simulation:

The temperature field was simulated using the Heat Transfer in Solids module in COMSOL Multiphysics, solving the steady-state heat conduction equation:

$$\nabla \cdot (k\nabla T) = 0$$

The model consists of a multilayer structure corresponding to the device geometry. The thermal conductivity of the liquid metal (Ga–In alloy) was taken from the material library in COMSOL, while the effective thermal conductivity of the Ecoflex–Al_2O_3 composite layer was calculated using an effective medium approximation (Maxwell–Garnett model).

A constant heat power was applied at the bottom copper heat source. The top surface was subjected to natural convection and thermal radiation to ambient air (25 °C), with a convection coefficient of 10 W m^{-2} K^{-1} and emissivity defined according to each material. The side boundaries were set as adiabatic, assuming negligible lateral heat loss.

The mesh was generated using a physics-controlled fine mesh, with local refinement applied at material interfaces to ensure numerical accuracy.

S4: Thermal diffusivity coefficients models:

The device was modeled as a bilayer structure consisting of an Ecoflex–Al_2O_3 composite layer and a liquid-metal layer. Under tensile strain, the composite layer thickness was assumed to decrease as $t_1 = t_{1,0}/(1+\varepsilon_0)$, where ε_0 is the applied uniaxial engineering strain, defined as $\varepsilon_0 = (L - L_0)/L_0$, with L_0 and L being the initial and

stretched lengths, respectively. Based on this geometry, the cross-plane conductivity was calculated using a series thermal-resistance model, and the in-plane conductivity was calculated using a parallel conduction model[3,4]:

$$k_{\perp} = \frac{t_1 + t_2}{t_1/k_1 + t_2/k_{lm}}, k_{\parallel} = \frac{t_1 k_1 + t_2 k_{lm}}{t_1 + t_2}$$

The corresponding equivalent thermal diffusivities were obtained from

$$\alpha = \frac{k}{\rho C_p}$$

using the thickness-weighted average volumetric heat capacity of the bilayer. The in-plane characteristic diffusion time was further estimated from $\tau_{\parallel} = L_{\text{char}}^2/\alpha_{\parallel}$.

S5: Calculation of dicrotic-notch identifiability index:

We introduced the **dicrotic-notch identifiability index**, which was defined as the percentage of pulse cycles in which the dicrotic notch could be clearly identified:

$$\text{Dicrotic-notch identifiability index} = \frac{N_{\text{DN}}}{N_{\text{total}}} \times 100\%$$

where N_{DN} is the number of pulse cycles with an identifiable dicrotic notch, and N_{total} is the total number of analyzed pulse cycles. A higher value therefore indicates better preservation of the fine morphological features of the PPG waveform.

Supplementary Table 1. Comparison of solar reflectance, mid-infrared emissivity, and stretchability of SPCI with flexible/stretchable radiative cooling materials.

Work	Reflectance (%)	Emittance (%)	Stretchability (%)
This work (SPCI)	92.6	90	>800
USRI[5]	91	97	10
SRCM[6]	98	NA	50
UP bioelectrodes[7]	95.8	93.1	NA

REFERENCE

[1] Palik, E. D. *Handbook of Optical Constants of Solids.* Academic Press: San Diego, **1998**.

[2] Yalçın, R. A.; Blandre, E.; Joulain, K.; et al. Colored Radiative Cooling Coatings with Nanoparticles. *ACS Photonics* **2020**, *7(5)*, 1312-1322. DOI: 10.1021/acsphotonics.0c00513.

[3] Philip, J. R.; de Vries, D. A. Moisture movement in porous materials under temperature gradients. *Trans. Am. Geophys. Union* **1957**, *38(2)*, 222-232. DOI: 10.1029/TR038i002p00222.

[4] Kim, S. H.; Anand, N. K. Laminar developing flow and heat transfer between a series of parallel plates with surface mounted discrete heat sources. *Int. J. Heat Mass Transf.* **1994**, *37(15)*, 2231-2244. DOI: 10.1016/0017-9310(94)90366-2.

[5] Li, J.; Fu, Y.; Zhou, J.; et al. Ultrathin, soft, radiative cooling interfaces for advanced thermal management in skin electronics. *Sci. Adv.* **2023**, *9(14)*, eadg1837. DOI: 10.1126/sciadv.adg1837.

[6] Dong, J.; Peng, Y.; Zhang, Y.; et al. Superelastic Radiative Cooling Metafabric for Comfortable Epidermal Electrophysiological Monitoring. *Nano-Micro Lett.* **2023**, *15(1)*, 181. DOI: 10.1007/s40820-023-01156-9.

[7] Peng, Y.; Dong, J.; Zhang, Y.; et al. Thermally comfortable epidermal bioelectrodes based on ultrastretchable and passive radiative cooling e-textiles. *Nano Energy* **2024**, *120*, 109143. DOI: 10.1016/j.nanoen.2023.109143.